Nonlinear inductive response of pinned superconducting vortices in artificial pinning sites

A. Al Luhaibi,[1,2,*] A. Glatz,[3,4,†] and J. B. Ketterson[1,‡]

[1] *Department of Physics and Astronomy, Northwestern University, Evanston, Illinois 60208, USA*
[2] *Physics Department, King Fahd University of Petroleum and Minerals, Dhahran 31261, Saudi Arabia*
[3] *Materials Science Division, Argonne National Laboratory, 9700 South Cass Avenue, Argonne, Illinois 60439, USA*
[4] *Department of Physics, Northern Illinois University, DeKalb, Illinois 60115, USA*

(Received 29 December 2023; revised 19 March 2024; accepted 4 April 2024; published 8 May 2024)

Using the time dependent Ginzburg-Landau equations, we simulate the inductive responses of a variety of thin-film systems containing patterned antidots with different sizes and shapes. The results for all shapes show that the kinetic inductance diverges as the applied current approaches a critical current that is below the BCS depairing current. Exploiting the similarity of the observed current-voltage behavior to that of Josephson junctions, we obtain an empirical equation that well fits the inductivity curve as a function of the applied current.

DOI: 10.1103/PhysRevApplied.21.054018

I. INTRODUCTION

At $T = 0$ the response of a superconductor is primarily reactive, X_s, for an externally applied alternating current with frequency $f_{\text{ext}} < \Delta/h$, where Δ is the energy gap and h is Plank's constant. This is referred to as "kinetic inductance" since it involves the kinetic energy of the moving condensate. The nonlinear proprieties of the kinetic inductance have attracted much interest due to potential applications in quantum sensing and other technologies involving superconducting wires and films [1]. Furthermore, superconducting vortices also show a reactance X_s that in the vicinity of a frequency f_d referred to as the "depinning frequency" crosses over to being resistive, R_s, due to the dissipation of moving vortex cores [2]. The explanation for such a response is that the disorder generally pins the vortices, resulting in a largely reactive response below f_d. Coffey and Clem [3] studied the response within the linear regime of a pinning potential with a model, now referred to as the "Coffey-Clem model," that generally agrees well with experiments. Van der Beek *et al.* [4] studied the nonlinear responses in a mixed state in the presence of defects using London's equations. Recently, Sauls [5] proposed a theory for nonlinear current responses in an inhomogeneous s-wave superconducting state in the absence of an applied field.

Holelike artificial periodic pinning sites in an applied field combine effects arising from both spatial inhomogeneity and a circulating supercurrent arising from flux quanta pinned in the holes. Such systems may be incorporated into various quantum circuits and can function as nonlinear inductors. In this work, we model the superconducting response of vortices at holelike pinning sites in commensurate magnetic fields (those where the ratio of the number of vortices to holes involves an integer) using the time-dependent Ginzburg-Landau (TDGL) equations, from which we can extract the effective (kinetic) inductivity; see Sec. II. In Secs. III and IV, we present and discuss the results obtained from the TDGL simulations of the inductive response as a function of an applied current. Details of the nonlinear behavior of the system are described in Sec. IV E. Possible uses of such devices as circuit elements are discussed in Sec. V.

II. MODEL

In the following three subsections, we first give a brief review of the response of a superconductor to an alternating current, then describe our model and computational approach using TDGL simulations following the work in Ref. [6], and finally introduce the method used to determine the reactance from the simulation results.

A. ac response

The Mattis-Bardeen theory describes the linear response of a superconductor to an electromagnetic field for frequencies f both above and below the energy gap Δ in

*Corresponding author: aalluhaibi@kfupm.edu.sa
†Corresponding author: glatz@anl.gov
‡Corresponding author: j-ketterson@northwestern.edu

the absence of an applied static magnetic field. Gao *et al.* [7] showed that under certain conditions an analytic solution of the Mattis-Bardeen theory can be obtained. In particular, for very low frequencies and temperatures compared with Δ, the real and imaginary parts of the complex conductivity, $\sigma = \sigma_1 + i\sigma_2$, can be written as

$$\frac{\sigma_1}{\sigma_n} = \frac{4\Delta}{hf} e^{-\frac{\Delta-\mu^*}{k_B T}} \sinh\left(\frac{hf}{2k_B T}\right) K_0\left(\frac{hf}{2k_B T}\right), \quad (1)$$

$$\frac{\sigma_2}{\sigma_n} = \frac{\pi\Delta}{hf}\left[1 - e^{-\frac{\Delta-\mu^*}{k_B T}} e^{\frac{hf}{2k_B T}} I_0\left(\frac{hf}{2k_B T}\right)\right], \quad (2)$$

where σ_n is the normal conductivity, μ^* is the chemical potential, and I_0 and K_0 are the zeroth-order modified Bessel functions of the first and second kind, respectively.

At absolute zero temperature, $\sigma = i\sigma_2$, implying a completely reactive response $X_s = (hf/\pi\Delta\sigma_n)(l/wd)$, implying a kinetic inductance $\mathcal{L}_k = (\hbar/\sigma_n\pi\Delta)(l/wd)$, where l, w, and d are the dimensions of the sample: length, width, and thickness, respectively. Since $\mathcal{L}_k \sim 1/\Delta$, a change of the energy gap by any means (such as a change of the temperature, magnetic field, or applied current) changes the kinetic inductance, as discussed in Ref. [8] as well as in Ref. [3], where the latter involves pinned vortices.

The idea explored here is to use the dynamic response of pinned flux quanta in antidots (holes or localized vacant regions) placed within a superconducting film. Although these flux quanta do not have cores like conventional vortices, their motion still modulates the order parameter and larger currents can increase the nonlinearity in kinetic induction. Furthermore, the absence of normal cores lowers the dissipation. Pinned vortices in artificial pinning sites would be quite complex to treat via methods analogous to those used by Mattis and Bardeen [9] and therefore we use the TDGL equations to numerically study the dynamic vortex responses of hole arrays.

B. TDGL simulations

The TDGL equations for the order parameter $\psi(\mathbf{r})$ may be written as [6]

$$-\Gamma\left(\partial_t + i\frac{2e}{\hbar}\mu\right)\psi = -a\psi + b|\psi|^2\psi - \frac{1}{4m}\left(\hbar\nabla + \frac{2e}{ic}\mathbf{A}\right)^2\psi, \quad (3)$$

$$\nabla\times\nabla\times\mathbf{A} = \frac{4\pi}{c}\left(\mathbf{J}_s + \mathbf{J}_n\right), \quad (4)$$

where e and m are the electron charge and mass, respectively, c is the speed of light in a vacuum, μ and $\mathbf{A}$ are the scalar and vector potentials, Γ, a, and b are material dependent parameters, and $\mathbf{J}_n$ and $\mathbf{J}_s$ are the normal and superconducting current densities given by

$$\mathbf{J}_n = -\sigma\left(\nabla\mu + \frac{1}{c}\partial_t\mathbf{A}\right), \quad (5)$$

$$\mathbf{J}_s = -\frac{e}{2m}\left[\psi^*\left(i\hbar\nabla + \frac{2e}{c}\mathbf{A}\right)\psi + \text{c.c.}\right]. \quad (6)$$

These equations contain two fundamental length scales: the London penetration depth, $\lambda_L(T) = \lambda_{L,0}(1 - T/T_c)^{-1/2}$, and the coherence length, $\xi(T) = \xi_0(1 - T/T_c)^{-1/2}$; here $\lambda_{L,0}^2 = m_e c^2/8\pi e^2\psi_0^2$, with $\psi_0^2 = a/|b|$, and $\xi_0^2 = \hbar^2/4ma_0$. In constructing dimensionless equations, Sadovskyy *et al.* [6] used the zero-temperature coherence length ξ_0 as the unit of length such that the geometry of inclusions in the superconductor is temperature independent. The second length is then incorporated through the dimensionless ratio $\kappa = \lambda_0/\xi_0$, the Ginzburg-Landau parameter. The unit of time chosen, reflecting the effect of σ_n through $\mathbf{J}_n$, is $t_0 = \sigma_n m_e/2e^2\psi_0^2$. Γ, which also affects the time evolution, enters via a second dimensionless ratio $u = \Gamma/\nu_0 t_0$. With these definitions the TDGL equations can be written in dimensionless form as

$$u(\partial_t + i\mu)\psi = \epsilon(\mathbf{r})\psi - |\psi|^2\psi + (\nabla - i\mathbf{A})^2\psi, \quad (7)$$

$$\kappa^2\nabla\times(\nabla\times\mathbf{A}) = \mathbf{J}_s + \mathbf{J}_n, \quad (8)$$

where $\epsilon(\mathbf{r}) \equiv (T_c(\mathbf{r}) - T)/T$.

The magnetic field, and correspondingly the vector potential, is measured in the unit of the upper critical field $H_{c2}(T=0) = \phi_0/2\pi\xi_0^2$ ($\phi_0 = \pi\hbar c/e$ is the flux quantum). The total current density can be written as

$$\mathbf{J} = \mathbf{J}_s + \mathbf{J}_n = \text{Im}\left[\psi^*(\nabla - i\mathbf{A})\psi\right] - (\nabla\mu + \partial_t\mathbf{A}), \quad (9)$$

where the unit of the current density is given by $J_0 = (e\hbar/m_e\xi_0)\psi_0^2$. In these units, the depairing current density J_{dp} has the value $2/\sqrt{27} \approx 0.385$.

One can model the pinning strength of metallic inclusions by so-called δT_c pinning [10], where the critical temperature is spatially modulated. In Eq. (7), this is realized through the coefficient of the linear Ginzburg-Landau term. In the superconductor we use $\epsilon = 1$ and within the pinning site we use $\epsilon < 1$; i.e., the local critical temperature of the pinning site is less than the bulk T_c. For $0 < \epsilon < 1$, one has weakened superconducting defects, whereas regions with $\epsilon < 0$ model normal defects. To model actual holes (antidots), which are discussed here, we impose internal no-current or open boundary conditions at their perimeter, $(\nabla - i\mathbf{A})\psi\cdot\hat{\mathbf{n}} = 0$, where $\hat{\mathbf{n}}$ is the normal vector of the boundary. This ensures that no current passes through the defect. An external current density is applied

in the x direction of the form

$$J_{\mathrm{ext},x}(t) = J_{\mathrm{dc}} + J_{\mathrm{ac}} \sin(2\pi f_{\mathrm{ext}} t). \tag{10}$$

In the following we drop the subscript x and assume that the external current and the resulting electric field E across the sample are in the x direction. The electric field E results in a linear contribution to the scalar potential, such that we can write $\mu = -xE + \tilde{\mu}(\mathbf{r})$, where $\tilde{\mu}(\mathbf{r})$ is a periodic function describing the deviations of the scalar potential from the linear part fulfilling the Poisson equation. With the gauge transformation $\psi(\mathbf{r}) = \tilde{\psi}(\mathbf{r}) e^{i\Phi x}$, we can solve the TDGL equations numerically with quasiperiodic boundary conditions for $\tilde{\psi}$ in the x direction; see Ref. [6]. Here Φ can be interpreted as an effective flux (Sec. V A), since $E = \partial_t \Phi$, and its value is determined by the differential equation

$$\begin{aligned} J_{\mathrm{ext}}(t) &= \langle J_x(\mathbf{r}) \rangle \\ &= \mathrm{Im}\left(\left\langle \tilde{\psi}^* (\partial_x + i\Phi - iA_x) \tilde{\psi} \right\rangle \right) + \partial_t \Phi - \langle \partial_t A_x \rangle, \end{aligned}$$

which requires the calculation of the sample-averaged x component of the current density $\langle J_x(\mathbf{r}) \rangle$ at each time step when one is solving the TDGL equations numerically.

It is important to note that the TDGL formalism is valid as long as nonequilibrium excitations are small and the system remains in a near steady state. Therefore, we consider only frequencies $f_{\mathrm{ext}} \ll \Gamma^{-1} = \tau_\psi^{-1}$, with Γ obtained from the microscopic theory as $\Gamma = \nu_0 \pi \hbar / 8 k_B T_c$, where ν_0 is the density of states. Furthermore, we must keep the peak applied current density $J_{\mathrm{dc}} + J_{\mathrm{ac}}$ well below the depairing current density so order parameter fluctuations can be ignored. For a more-detailed discussion of nonequilibrium effects, we refer the reader to the book by Kopnin [11].

For the numerical solution of Eq. (7), the system is discretized on a regular two-dimensional mesh in space (with a typical grid spacing of $0.3\xi_0$) with (quasi)periodic boundary conditions and the time integration is performed by our using an implicit Crank-Nicolson scheme (typical time discretization $0.1 t_0$). These discretized equations are then simulated on graphics-processing units with use of an iterative Jacobi solver.

Because of the periodic boundary conditions, the systems studied here represent superconducting films with a periodic array of holes (see Fig. 1) having superlattice spacing L (the linear size of the unit cell). The holes themselves are either circular (with diameter D) or triangular (an isosceles triangle with side S and base B, or an equilateral triangle with side S).

C. Method

The impedance of type-II superconductors was studied in earlier work, starting with Gittleman and Rosenblum (GR) (see Refs. [2,3,12]), in systems of pinned vortices with use of an equation of motion involving a harmonic restoring force (a spring) along with viscous damping (proportional to the velocity). The associated dynamics is equivalent to an electrical circuit involving an inductor and a resistor in parallel; with increasing frequency, the response crosses over from inductive to resistive at a frequency f_d referred to as the "depinning frequency."

The TDGL-simulation output is the spatially averaged electric field over the simulated system, E, that results from the applied external current density J_{ext}. The ratio of E to J_{ext} is taken to be a spatial averaged specific impedance ζ. For our parallel-circuit model, it corresponds to a spatial averaged resistivity ρ and the inductivity λ combined according to $\zeta_{\mathrm{GR}} = (\rho^{-1} + (i2\pi f_{\mathrm{ext}} \lambda)^{-1})^{-1}$; both components can be nonlinear with applied current density. In the limit of small J_{ext}, ζ can be represented by its magnitude $|\zeta|$ and the phase θ, which for our parallel model is given by

$$|\zeta_{\mathrm{GR}}| = \frac{2\pi f_{\mathrm{ext}} \lambda}{\sqrt{1 + (f_{\mathrm{ext}}/f_d)^2}}, \tag{11}$$

$$\theta_{\mathrm{GR}} = \arctan\left(f_d / f_{\mathrm{ext}}\right), \tag{12}$$

where $f_d = \rho / 2\pi\lambda$.

For $f_{\mathrm{ext}} \ll f_d$, the response is primarily reactive, which largely arises from the kinetic energy of the condensate, and is determined as a function of the bias current J_{dc} as follows: We introduce a (nonlinear) inductivity λ according to

$$E = \lambda(J_{\mathrm{ext}}) \frac{dJ_{\mathrm{ext}}}{dt}. \tag{13}$$

One can then write $\lambda(J_{\mathrm{ext}})$ as an expansion,

$$\lambda(J_{\mathrm{ext}}) = \lambda_0 + \sum_{n=1}^{\infty} \alpha_n J_{\mathrm{dc}}^n \left[1 + \frac{J_{\mathrm{ac}}}{J_{\mathrm{dc}}} \sin(2\pi f_{\mathrm{ext}} t) \right]^n. \tag{14}$$

λ_0 in Eq. (14) characterizes the linear response and α_n are expansion coefficients, which parameterize the nonlinear contribution to λ. In the limit of $J_{\mathrm{ac}}/J_{\mathrm{dc}} \ll 1$, we can write Eq. (13) as

$$E = 2\pi f_{\mathrm{ext}} \lambda_{\mathrm{eff}}(J_{\mathrm{dc}}) J_{\mathrm{ac}} \sin(2\pi f_{\mathrm{ext}} t + \theta), \tag{15}$$

where θ is the phase shift of the electric field with respect to the applied current and λ_{eff} an effective, small-amplitude dynamic inductivity in the presence of a large direct current:

$$\lambda_{\mathrm{eff}}(J_{\mathrm{ext}}) = \sum_{n=0}^{\infty} \alpha_n J_{\mathrm{dc}}^n. \tag{16}$$

Here the summand $n = 0$ corresponds to the linear response, i.e., $\alpha_0 = \lambda_0$. For the inductive response, E and

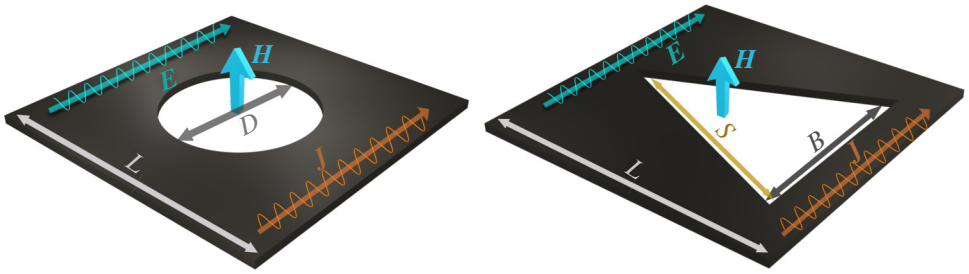

FIG. 1. Unit-cell geometry used for the simulation. The white spot is the hole. Here it is a circular hole with diameter D (left) or an isosceles-triangular hole with base B and side S (right). **H** is the magnetic field direction perpendicular to the superconducting film and L is the linear size of the square unit cell. **J** is the current density and **E** is the electric field applied in the x direction. The wavy lines over the current density and electric field arrow indicate the ac response. In the isosceles-triangular hole, the applied current density **J** is parallel to the base B. The boundary conditions in the simulations are periodic.

$J_{\rm ext}$ are orthogonal ($\theta = \pi/2$), but we discuss the case of $\theta < \pi/2$ as well below.

III. RESULTS

Figure 2 shows λ versus the direct-current density for two cases of circular holes. Also shown are results for an equilateral triangle (with sides $S = 5$ in the unit of ξ_0) and an isosceles triangle (with base $B = 3$ and sides $S = 6$); the latter two cases are shown, separately, for when the Lorentz force pushes the vortex toward the apex of the triangle and when it is pushed toward the base, the latter having the higher critical current. The simulations show an overall similar behavior of λ in that it increases slowly at first, followed by a rapid rise as $J_{\rm dc}$ approaches J_c, as seen in Fig. 2. Near J_c, a rapid rise is expected in a uniform system since $\lambda_k \sim \Delta^{-1}$; in that case, J_c is $J_{\rm dp}$ for a clean uniform superconductor with no applied field. However, here it occurs at the depinning current for antidot defects. Note that in Fig. 2, the inductivity of triangular antidots shows an asymmetric behavior in J_c. An asymmetry in the critical current for triangular pinning sites was observed by Villegas *et al.* [13] while, to our knowledge, such behavior in the inductivity has not been studied. Hence, the shape of the pinning potential along the direction of the Lorentz force plays an essential role in the inductivity of the system. It can also be seen in Fig. 3 that changing the number of pinned flux quanta per unit cell or hole, n_ϕ, not only changes J_c but also affects the behavior of λ as a function of $J_{\rm dc}$.

Figure 2 also shows that the initial, constant, part of the inductivity λ_0 increases with the hole diameter due to the reduction of the order parameter caused by the reduced superconducting fraction of the system with increasing hole diameter.

Figure 3 shows λ versus $J_{\rm dc}$ for a square unit cell with linear size $L = 10$ containing a hole with diameter $D = 7.5$ for different numbers n_ϕ of trapped vortices. We see that λ_0 increases with the applied field and appears to diverge as the applied field approaches H_{c2}. Note that J_c decreases, as expected, since Δ locally decreases with increasing applied magnetic field.

Figure 3 also shows the coefficient λ_0 governing the linear regime for increasing values of the trapped vorticity per hole n_ϕ.

In our simulations we use $\epsilon = 1$ within the superconductor, i.e., a ratio $T/T_c = 1/2$. The value of ϵ mostly determines the critical current J_c. However, our results hold as long as the effect of $J_{\rm ac}$ on the order-parameter dynamics is larger than the effect of thermal fluctuations, which are determined by the absolute temperature, and not the value of ϵ. These would be included as additive noise term in Eq. (7); see Ref. [6]. Here we consider sufficiently

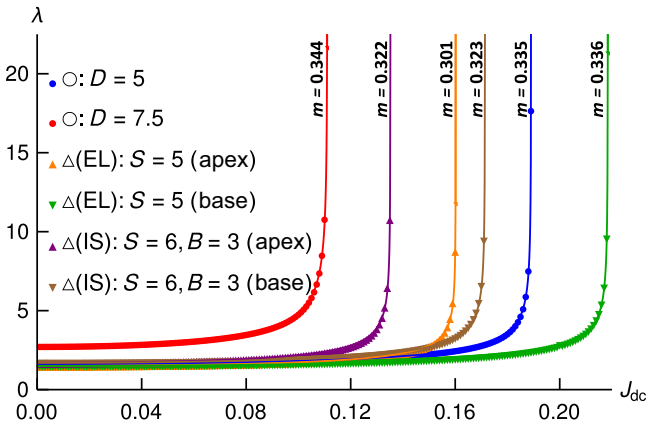

FIG. 2. Inductivity λ versus applied direct current $J_{\rm dc}$ for $J_{\rm ac} = 10^{-6}$ and $f_{\rm ext} = 4 \times 10^{-4}$ for a single vortex pinned in a system with a unit cell of length $L = 10$ containing a hole with differing shapes as described in the legend. Simulation data points are marked by the corresponding symbols in the legend, while lines with the same colors represent fits to Eq. (17) with the exponent m given in the graph. EL, equilateral triangle; IS, isosceles triangle.

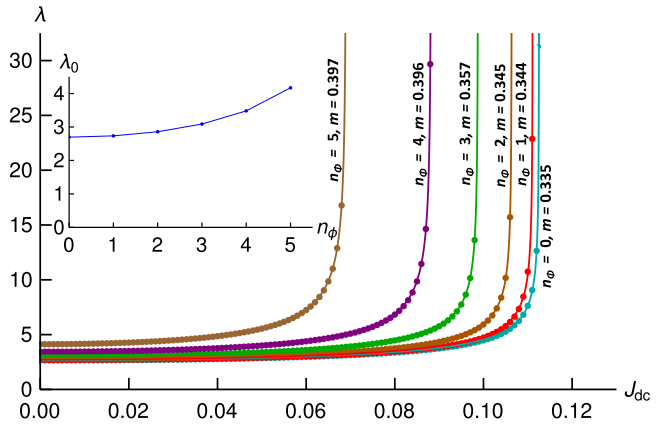

FIG. 3. Inductivity λ versus applied direct current J_{dc} for $J_{ac} = 10^{-6}$ and $f_{ext} = 4 \times 10^{-4}$ for a system with linear unit-cell size $L = 10$ containing a circular hole with diameter $D = 7.5$. The number of pinned flux quanta n_ϕ is different for each graph and is marked next to them. Simulation data points are marked by symbols, while lines with the same colors represent fits to Eq. (17) with the exponent m given in the graph.

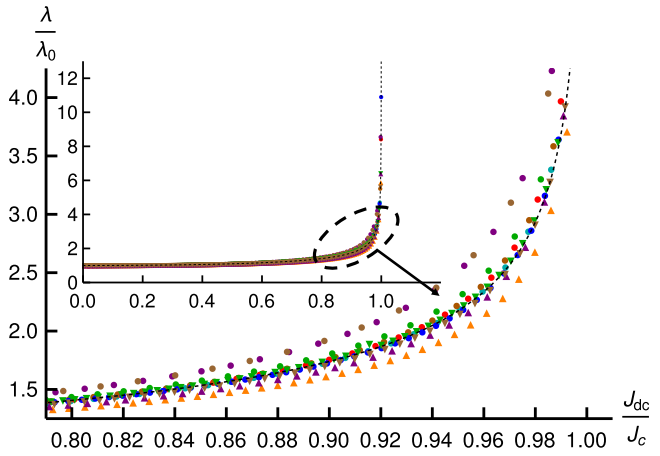

FIG. 4. Normalized inductivity versus normalized applied direct current for all systems in Figs. 2 and 3 with the same colors and symbols as in Figs. 2 and 3. The dashed black line is a plot of Eq. (17) with $m = \frac{1}{3}$.

low temperatures, such that the effect of thermal noise can be ignored.

IV. DISCUSSION

A. Phenomenological model

Figures 2 and 3 show similar behaviors: λ initially increases slowly but rises rapidly near J_c. The E-J curves explored suggest a divergence of the impedance before J_c (thermal activation, leading to flux creep, is suppressed in our calculations). Guided by the kinetic inductance of Josephson junctions in which the exponent m is equal to 0.5, we fit our simulations for $\lambda(J)$ to the following empirical expression:

$$\lambda^* = \lambda_0 \left[1 - \left(\frac{J}{J_c} \right)^2 \right]^{-m}, \tag{17}$$

where m is a fitting parameter that depends on various factors, as can be seen in Figs. 2 and 3, and J_c is a critical current marking the onset of dissipation via some other mechanism, such as vortex depinning or vortex-antivortex-pair creation. Figure 4 shows the normalized results from Figs. 2 and 3. The dashed black line is a fit of Eq. (17) with $m = 1/3$. Clearly this form gives a good overall representation of the simulated behavior, although there is no evidence that the exponent m is universal.

A natural question is what generates the observed responses. In this connection, Beenakker and van Houten [14] examined a constriction in a superconducting film having a slowly varying width and showed it can exhibit an effect similar to that in a Josephson junction wherein an applied current causes the phase Θ to change between the two ends of the constriction. Vortices trapped in holes (which generate the necks) will alter the current-density distribution in the necks, which changes the inductivity, in an ultimately nonlinear way, when displaced by the direct current; this, in turn, strongly shifts the phase. A dynamic variation of the current will then generate a time-dependent phase and with it a voltage.

Focusing on the circular holes, we see that the change of the system dimensions (L and D) has an influence on the inductivity parameters in Eq. (17) (λ_0, m, and J_c). Figure 5 shows the behavior of the inductivity parameters when L and D are changed for fixed $D = 5$ and $L = 10$, respectively. J_c behaves as expected with D by increasing until it reaches a maximum value, after which it starts decreasing [15]. The dependence on L is different from that on D, because with increasing L, the applied magnetic field decreases, which reduces the vortex-vortex interaction, which leads to asymptotic behavior as shown in Fig. 5. Qualitatively, the behavior of λ_0 is inversely proportional to the spatially averaged order-parameter amplitude $\langle|\psi|\rangle$ of the system, which can be understood as follows: changing D or L also changes the fraction of the superconducting area A_s or hole area A_h with respect to the total unit-cell area, $A_s/L^2 = 1 - A_h/L^2$, and with it the average order-parameter amplitude $\langle|\psi|\rangle$ (which is almost proportional apart from proximity effects). It follows that as A_s/L^2 decreases, λ_0 increases. This result qualitatively agrees with what was described in Sec. II A. Furthermore, the exponent m appears to increase slightly with increasing D and decrease with increasing L. Finally, the effective phase θ is determined by our fitting Eq. (15) together with the computed electric field amplitude; it depends on both the frequency and the applied current as shown in Fig. 7. The zero-current phase θ_0, which depends on the system geometry, is shown in Fig. 5.

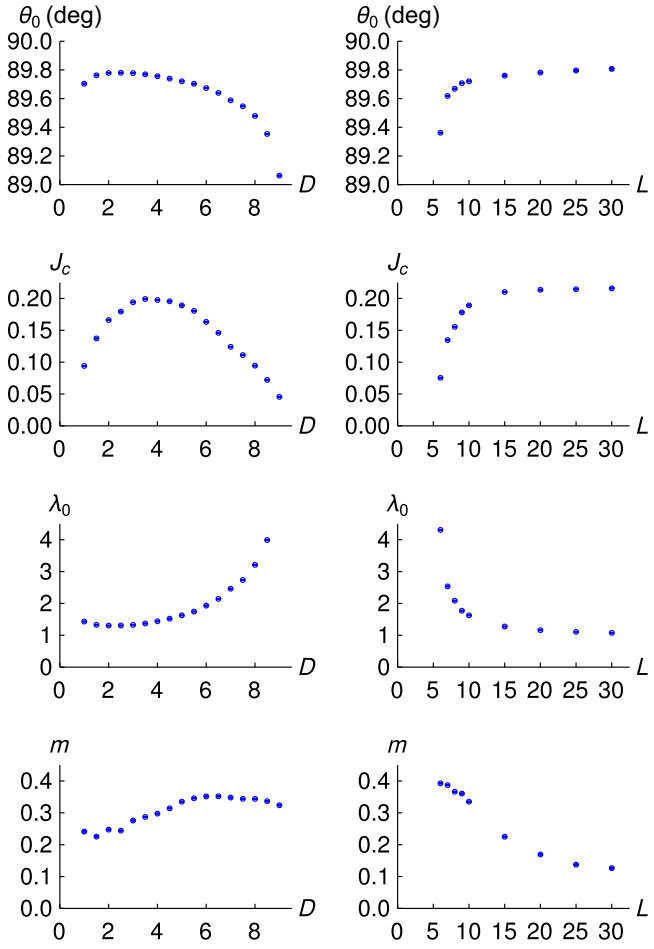

FIG. 5. Behavior of θ_0, J_c, λ_0, and m (from top to bottom) versus D for $L = 10$ (shown on the left) and versus L for $D = 5$ (shown on the right) for a system with a single pinned vortex and applied frequency $f_{\text{ext}} = 4 \times 10^{-4}$.

B. Frequency dependence

In the systems studied by Gittleman and Rosenblum [2], f_d was in the megahertz range and the data were well represented by their model both above and below f_d. In contrast, our vortices are more tightly bound, resulting in much-higher depinning frequencies than in the GR experiments and hence the GR model, where the dissipation was presumably governed by extrinsic mechanisms only (sample defects), is not expected to hold (see Sec. IV C), whereas our model has an additional intrinsic mechanism related to the order-parameter relaxation frequency, $f_d \sim \tau_\psi^{-1}$.

The calculations of λ were made under the assumption of $\theta \approx \pi/2$, i.e., the phase of the electric field and the current density differ by 90° [see Eq. (15)], which is reasonable since $f_{\text{ext}} = 4 \times 10^{-4} \ll f_d$ as implied from Fig. 5. For the system with $L = 10$ and $D = 9$, the lowest calculated depinning frequency $f_d = 0.02445 \lesssim \tau_\psi^{-1}$. Being near τ_ψ^{-1}, the GR predictions are not expected to follow the TDGL results. In Sec. IV C, we compare these models in more detail.

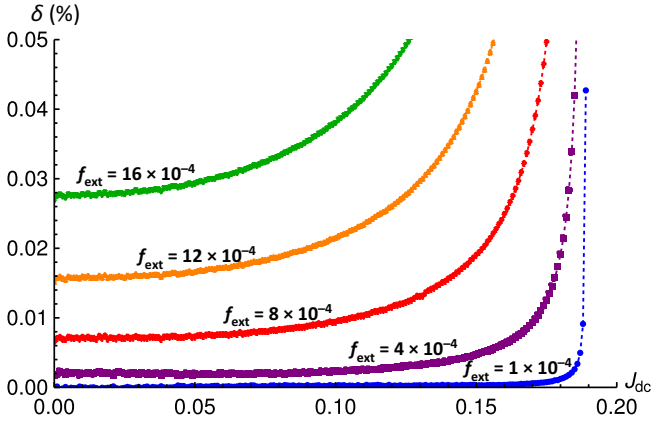

FIG. 6. Behavior of δ versus J_{dc} for the system with $L = 10$ and $D = 5$ for $f_{\text{ext}} = 1 \times 10^{-4}$ (blue), $f_{\text{ext}} = 4 \times 10^{-4}$ (purple), $f_{\text{ext}} = 8 \times 10^{-4}$ (red), $f_{\text{ext}} = 12 \times 10^{-4}$ (orange), and $f_{\text{ext}} = 16 \times 10^{-4}$ (green) relative to the zero-frequency limit.

f_{ext} influences ζ due to the frequency dependence of the phase, as suggested by the GR model. Figure 6 shows $\delta(J_{\text{dc}})$, the shift from unity of the ratio of the specific impedance, $\zeta(J_{\text{dc}}, f)$, to its value at zero frequency, $\lambda(J_{\text{dc}}, 0)$,

$$\delta = 1 - \frac{|\zeta(J_{\text{dc}})|}{2\pi f_{\text{ext}} \lambda(J_{\text{dc}})},$$

which was obtained by our extrapolating the different applied frequencies to zero using a quartic polynomial. Figure 7 shows $\theta(J_{\text{dc}})$ for different applied frequencies. It shows a stronger frequency dependence as well as a larger dependence on J_{dc}. For example, for $f_{\text{ext}} = 16 \times 10^{-4}$, $\theta_0 \approx 88.9°$ and $\theta(J_c) \approx 62°$, while for $f_{\text{ext}} = 1 \times 10^{-4}$, $\theta_0 \approx 89.9°$ and $\theta(J_c) \approx 89.5°$. This indicates that the higher frequencies strongly influence the system.

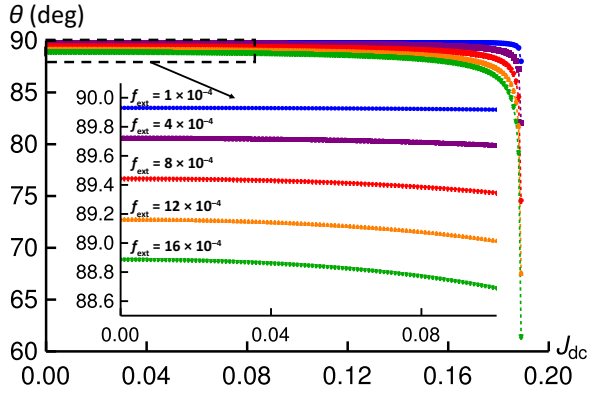

FIG. 7. Phase θ versus J_{dc} in the system with $L = 10$ and $D = 5$ for $f_{\text{ext}} = 1 \times 10^{-4}$ (blue), $f_{\text{ext}} = 4 \times 10^{-4}$ (purple), $f_{\text{ext}} = 8 \times 10^{-4}$ (red), $f_{\text{ext}} = 12 \times 10^{-4}$ (orange), and $f_{\text{ext}} = 16 \times 10^{-4}$ (green).

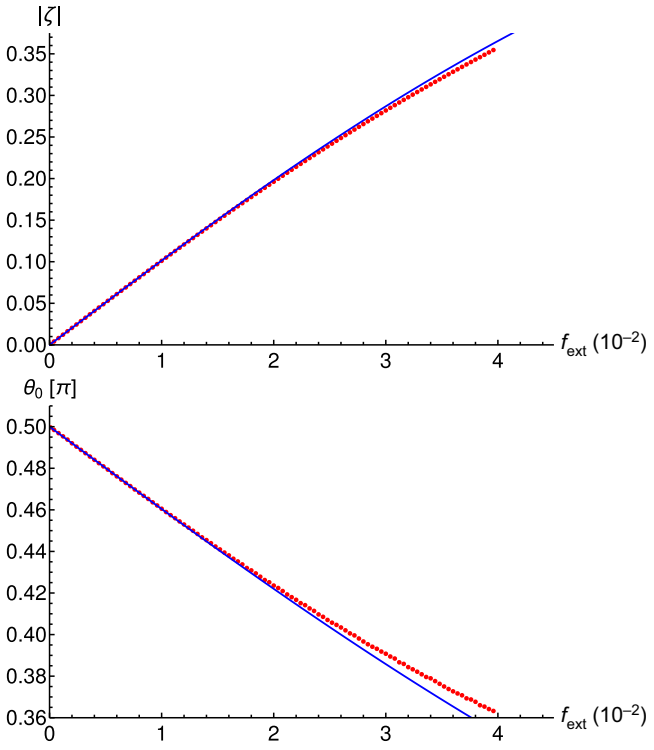

FIG. 8. Behavior of $|\zeta|$ (top) and θ_0 (bottom) versus f_{ext}. The red data points are from the TDGL simulation and the blue line is the prediction of the GR model. One can see the line fits the simulation data very well for $f_{ext} < 0.01$. For $f_{ext} > 16 \times 10^{-4}$, the typical time discretization becomes $0.01t_0$.

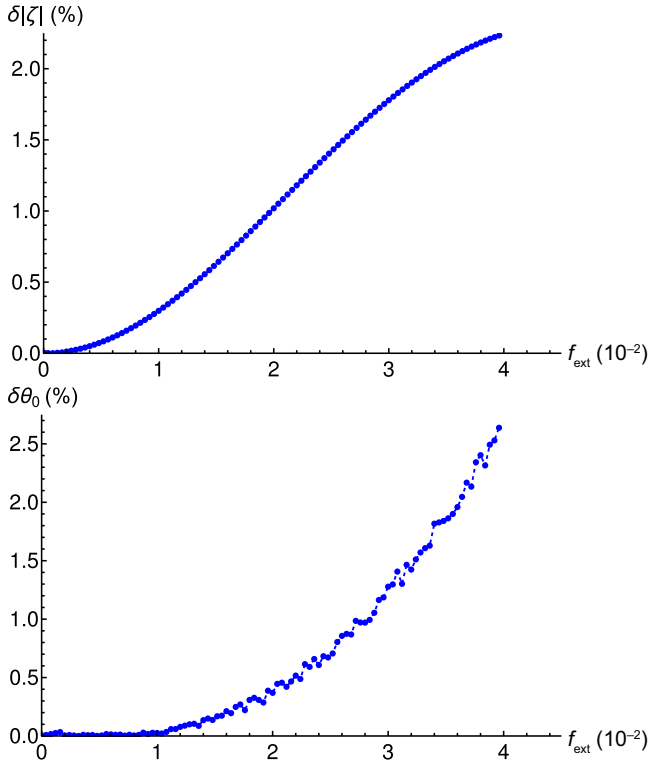

FIG. 9. Behavior of the relative error of TDGL and GR models $\delta|\zeta|$ (top) and $\delta\theta_0$ (bottom) versus f_{ext}. For $f_{ext} > 16 \times 10^{-4}$, the typical time discretization becomes $0.01t_0$.

C. Testing the Gittleman-Rosenblum model

On the basis of Fig. 6 for our system with $L = 10$ and $D = 5$, θ_0, which is proportional to ρ, starts from $\frac{\pi}{2}$ and decreases linearly with increasing f_{ext}. This is similar to the behavior of a parallel resistor-inductor circuit, which is what Gittleman and Rosenblum [2] consider in their model. When we fit the TDGL data in the limit of small J and small f_{ext}, we obtain $\lambda(J_{dc} = 0) = 1.62563$, using quartic polynomial extrapolation to zero frequency of $|\zeta(J_{ext})|/2\pi f_{ext}$, and $\rho = 0.817060$ by fitting Eqs. (11) and (12) simultaneously for f_{ext} up to 4×10^{-3}, which can be considered a low-frequency limit. From these values, we can plot $|\zeta_{GR}|$ and θ_{GR} versus f_{ext} [Eqs. (11) and (12), respectively]. The blue line in Fig. 8 shows the prediction of the GR model, whereas the red points correspond to the TDGL simulation. Clearly, they depart at higher frequencies; the TDGL calculation has a stronger frequency dependence than the GR model. Figure 9 shows the relative error of the two plots in Fig. 8. It shows that the relative difference up to $f_{ext} = 0.0396$ is less than 3%, which tends to increase as f_{ext} increases.

It is worth noting that our value of ρ is much higher than the expected flux-flow resistivity, ρ_{FF}, which Gittleman and Rosenblum suggest should govern the high-frequency response, implying the antidot system is different.

We now comment on the enhanced frequency dependence implied by the GR fit to the TDGL simulations. Two parameters enter the left-hand side of Eq. (3) and control the relaxation of the order parameter: The first is the order-parameter decay rate Γ. The second arises from the chemical potential μ, which, in turn, involves the electrical field, the latter being connected to the normal current via the electrical conductivity σ. The frequencies involved in the GR experiments were low, in the megahertz range, so it is natural to assume the GR model is the dominant mechanism in that limit. This explains our good agreement with the GR model at low frequencies. Now Γ multiplies the operator ∂_t, which produces a response proportional to f_{ext} [16]; i.e. a stronger dependence than that associated with μ as the results shown in Figs. 8 and 9 imply.

D. Breaking inversion symmetry with triangular pinning sites

In Fig. 2, we show separate plots for the two different current directions for the equilateral-triangular and isosceles-triangular holes. Note the critical currents, as well as the exponent m, differ for the different current directions, a direct result of the breaking of inversion symmetry.

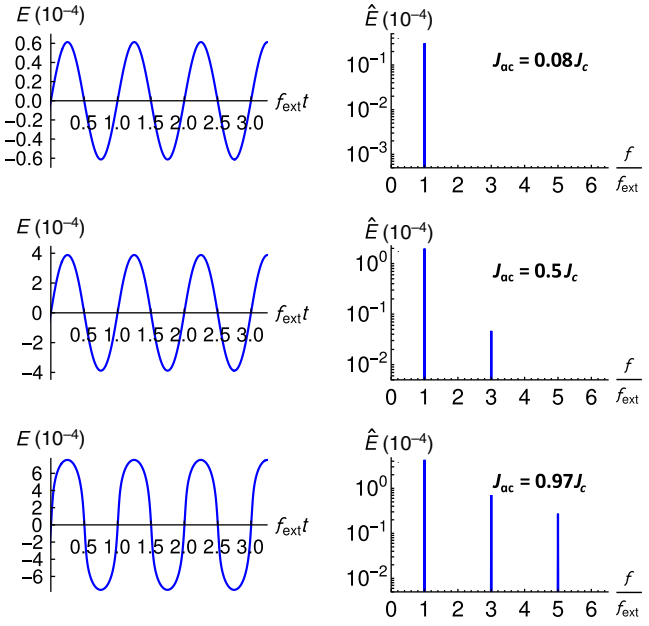

FIG. 10. ac response of a single pinned vortex in a system of size 10×10 with a circular hole of diameter $D = 5$ for different values of $J_{\rm ac}$ with $J_{\rm dc} = 0$.

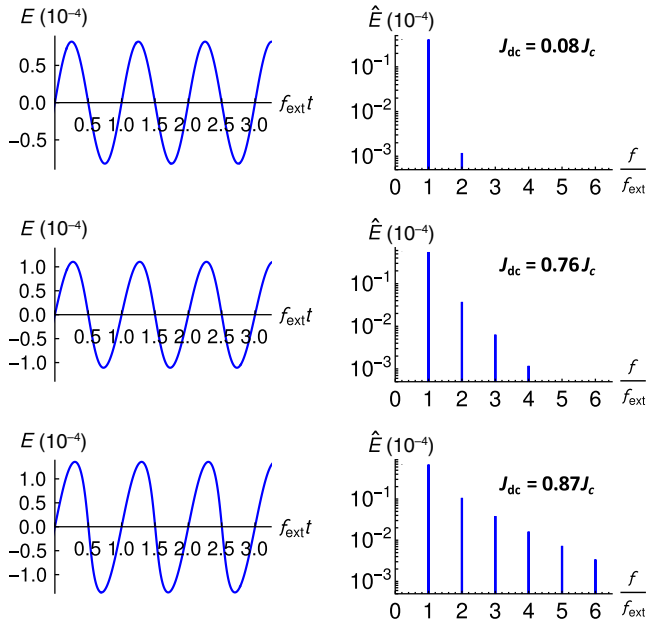

FIG. 11. ac response of a single pinned vortex in a system of size 10×10 with a circular hole of diameter $D = 5$ for different values of $J_{\rm dc}$ with $J_{\rm ac} = 0.02$.

For the equilateral triangle ($B = 5$ and $S = 5$), the difference between the two critical currents ΔJ_c is 0.058 and the difference between the exponents Δm is 0.035. For the isosceles triangle ($B = 3$ and $S = 6$) we have $\Delta J_c = 0.036$ and $\Delta m = 0.001$, i.e., the exponent m is almost unchanged. An asymmetry in the critical current is expected on the basis of the experiments by Villegas *et al.* [13]. However, the asymmetry in the exponent m is more surprising.

Equation (17) is an even function of J, which well fits the circular-hole inductivities in Fig. 2, while triangular shapes suggest an odd contribution. To partially compensate for this, we fit the upper part (apex) and the lower part (base) of the triangle separately, to retain the simple behavior of Eq. (17).

E. Nonlinear response

Figure 10 shows the electric field $E(t)$ arising from our applying a large-amplitude alternating current with $J_{\rm dc} = 0$ to a 10×10 system with a circular hole of diameter $D = 5$ containing a single vortex. Also shown in Fig. 10 is the Fourier transform $\hat{E}$ of the resulting $E(t)$; note that it contains only odd harmonics, as expected since the pinning potential profile has mirror symmetry about the current direction. However, by addition of a direct current as a tunable parameter, it is possible to excite both even and odd harmonics by breaking the mirror symmetry, as shown in Fig. 11. As discussed in Sec. IV D, the triangular antidots intrinsically break the mirror symmetry, thereby allowing the generation of even harmonics without the need to apply a direct current. Figure 12 shows the presence of odd and even harmonics, although the latter are weaker. Further optimization of the hole shapes, so as to enhance even harmonics, should be possible.

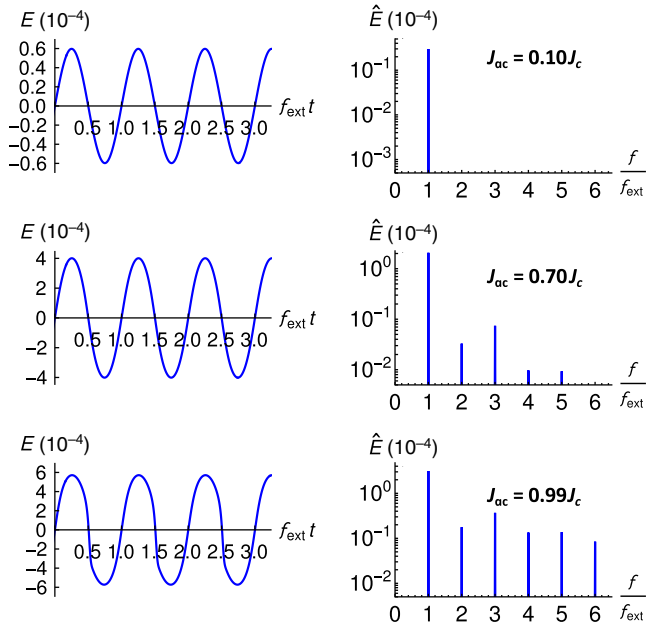

FIG. 12. ac response of a single pinned vortex in a system of size 10×10 for an isosceles-triangular hole with base $B = 3$ and side $S = 6$ for different values of $J_{\rm ac}$ with $J_{\rm dc} = 0$.

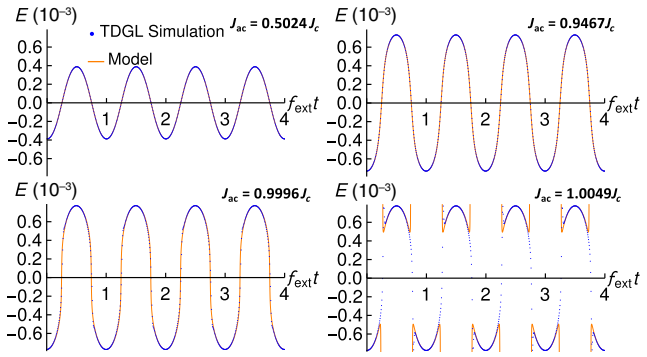

FIG. 13. Comparison between the model [Eq. (17)] and the TDGL simulation for different J_{ac} values for a circular pinning site with diameter $D = 5$ and unit-cell size 10×10 with a single pinned vortex. Here $\lambda_0 = 1.6256$, $J_c = 0.1891$, and $m = 0.3350$.

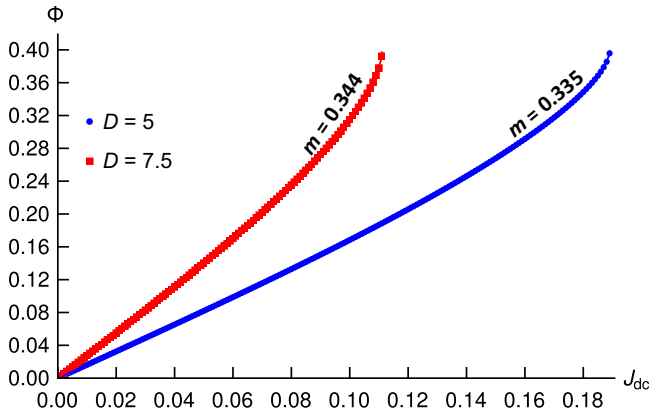

FIG. 14. Comparison of Φ from the TDGL simulation and Φ^* according to Eq. (18) versus J_{dc} for circular pinning sites with diameters $D = 5$ and $D = 7.5$ and a 10×10 unit cell with a single pinned vortex. The fitted line is almost indistinguishable from the simulation data.

V. ARTIFICIAL PINNING SITES AS CIRCUIT ELEMENTS

Nonlinear responses are an essential component of a variety cryogenic circuits applications, e.g., qubits [17] and rapid-single-flux-quantum logic circuits [18]. On the basis of calculations performed here, it would appear that hole-array-based devices deserve serious consideration wherever inductive components are required. In this connection Eq. (17) can be used to simplify modeling of the inductive response of artificial pinning sites as elements embedded in larger circuits. The second-order responses of the triangles and the current-biased circular holes might be exploited to make low-noise, cryogenic parametric amplifiers and oscillators [19]. Another possible application is in particle and photon detectors [20].

As noted above, and apparent from Figs. 2 and 3, the TDGL simulation is well represented by Eq. (17). For diameter $D = 5$ and lattice spacing $L = 10$, where the fit yields $J_c = 0.189$ and $m = 0.336$, the model matches the simulation quite well (see Fig. 13), provided J is not too close to J_c, at which point the vortex depins, giving way to the resistive response of a moving vortex, which is beyond the consideration of the model.

A. Effective flux and potential energy

The effective flux Φ produced by the current is quite useful in understanding the inductive response of quantum circuits; it is common to use the effective flux to represent the potential energy in the Lagrangian of such circuits, while the capacitance enters through the kinetic energy. One can then construct the Hamiltonian of the circuit and obtain the resulting energy levels after quantization [17]. Therefore, having an analytical form for the effective flux as a function of current may prove useful in exploring the possibility of using antidot arrays as nonlinear inductive elements. Having a representation for the potential energy of the system can be as important as the effective flux, since the potential energy can provide insight into the dynamics of the circuit.

An empirical expression for the flux per unit length Φ^* can be obtained from the inductivity as $\Phi^*(J) = \int_0^J \lambda^*(J')dJ'$, with λ^* given by Eq. (17). This integral can be evaluated for a general J_c and m as

$$\Phi^*(J) = J\lambda_0 \cdot {}_2F_1\left(\frac{1}{2}, m; \frac{3}{2}; \frac{J^2}{J_c^2}\right), \tag{18}$$

where ${}_2F_1$ is the hypergeometric function. A comparison of $\Phi(J_{dc})$ obtained from TDGL simulations with a fit of Φ^* according to this model is shown in Fig. 14 for circular pinning sites with diameters $D = 5$ and $D = 7.5$ in an $L = 10$ unit cell with a single pinned vortex.

The exponent m in Eq. (18) changes its functional behavior from a linear response (a constant kinetic inductor) at $m = 0$ to $\arcsin(J/J_c)$ at $m = 0.5$ (a Josephson junction).

Finally, using a similar approach, we can calculate the potential energy for the empirical model using $U^* = \int_0^J \lambda^*(J')J'dJ'$. This integral yields

$$U^*(J) = E_L \frac{\left[1 - \left(\frac{J}{J_c}\right)^2\right]^{1-m} - 1}{m - 1}, \tag{19}$$

where $E_L = \frac{1}{2}\lambda_0 J_c^2$ is the energy density for a linear inductor. Note that we assume $m < 1$, but empirically, the fitted values of m are less than 0.5.

By combining Eqs. (18) and (19), we can, in principle, obtain $U^*(\Phi^*)$. The eigenvalues of the Hamiltonian resulting from connecting a (nonlinear) hole-array inductor and a capacitor in parallel would not have constant level spacings and could thereby form the basis for a superconducting qubit. Furthermore, the large inductances

associated with our inductor might also be used to make smaller resonant circuits to replace, and reduce the size of, the triaxial strip-line resonators used in transmon qubits [21]. They might be useful also for Josephson transmission-line amplifiers [22,23], currently of interest in dark-matter searches [24].

B. Nonlinear kinetic induction in the SI unit

To calculate the induction value in the SI unit, we need to first change our unit for the inductivity to the SI unit, λ^{SI}. The relation is given by $\lambda^{\mathrm{SI}} = \rho_n t_0 \lambda$, where ρ_n is the normal resistivity.

We now consider a single unit cell, in which we calculate the sheet kinetic inductance in the SI unit, $\mathcal{L}_{\square}^{\mathrm{SI}}$, using the relation above, $\mathcal{L}_{\square}^{\mathrm{SI}} = R_{\square} t_0 \lambda$, where $R_{\square}$ is the sheet resistance. Since we have a square unit cell, the sheet resistance is the normal resistance R_N. To maintain superconductivity in thin films, the sheet resistance must be kept less than approximately $h/4e^2 = 6.45\ \mathrm{k}\Omega$ [25]; here we take $R_{\square} = 100$–$1000\ \Omega$, $\lambda \approx 1$, and $t_0 \approx 10^{-13}$ s, implying $\mathcal{L}_{\square}^{\mathrm{SI}} = 0.01$–$0.1$ nH.

The kinetic inductance in the SI unit is given by $\mathcal{L}_K^{\mathrm{SI}} = \mathcal{L}_{\square}^{\mathrm{SI}} l/w$, where l/w is the geometrical ratio of the film (the length to the width), and to obtain a large $\mathcal{L}_K^{\mathrm{SI}}$, the ratio must be large.

VI. CONCLUSION

We have shown that a heterogeneous superconducting film containing periodic defects can serve as a nonlinear inductor. Moreover, we were able to characterize the nonlinear inductivity by exploiting the similarity between the calculated E-J curves and the behavior of Josephson junctions, which diverges at the critical current density. The fitting parameter m, an exponent characterizing the behavior [see Eq. (17)] is not universal, and it depends on the geometry of pinning site and the vortex pinning number, as implied by Figs. 2 and 3. The harmonic content arising from a large-amplitude alternating current in a system having pinning sites with mirror symmetry about the current direction involves only odd harmonics, while in a system lacking this symmetry, both odd and even harmonics are excited. When $J_{\mathrm{dc}} \neq 0$, all harmonics were excited, even for shapes with mirror symmetry, and the direct current can be used as a control parameter.

These properties suggest devices based on hole arrays have the potential to be used as circuit elements in future quantum devices.

The hole arrays studied here can be compared with arrays of Josephson junctions. A typical Josephson junction consists of a superconductor-insulator-superconductor junction, while here we consider narrow superconducting bridges or constrictions between holes that act as weak links. These have properties similar to those of Josephson junctions, but have lower charge noise; see Ref [26]. Therefore, we expect that devices based on holes will have less noisy characteristics. Finally, we note that arrays of holes are easier to fabricate than arrays of Josephson junctions.

ACKNOWLEDGMENTS

This research was supported by the National Science Foundation under Grant No. 1905742 (J.B.K.), by the U.S. Department of Energy, Office of Science, Basic Energy Sciences, Materials Sciences and Engineering Division (A.G.), and through the computational resources and staff contributions provided for the Quest high-performance-computing facility at Northwestern University, which is jointly supported by the Office of the Provost, the Office for Research, and Northwestern University Information Technology. A.A.L. was supported through a scholarship provided by King Fahd University of Petroleum and Minerals.

[1] S. Zhao, S. Withington, D. J. Goldie, and C. N. Thomas, Nonlinear properties of supercurrent-carrying single-and multi-layer thin-film superconductors, J. Low Temp. Phys. **199**, 34 (2020).

[2] J. I. Gittleman and B. Rosenblum, Radio-frequency resistance in the mixed state for subcritical currents, Phys. Rev. Lett. **16**, 734 (1966).

[3] M. W. Coffey and J. R. Clem, Unified theory of effects of vortex pinning and flux creep upon the rf surface impedance of type-II superconductors, Phys. Rev. Lett. **67**, 386 (1991).

[4] C. Van der Beek, V. Geshkenbein, and V. Vinokur, Linear and nonlinear ac response in the superconducting mixed state, Phys. Rev. B **48**, 3393 (1993).

[5] J. Sauls, Theory of disordered superconductors with applications to nonlinear current response, Prog. Theor. Exp. Phys. **2022**, 033I03 (2022).

[6] I. Sadovskyy, A. Koshelev, C. Phillips, D. Karpeyev, and A. Glatz, Stable large-scale solver for Ginzburg–Landau equations for superconductors, J. Comput. Phys. **294**, 639 (2015).

[7] J. Gao, J. Zmuidzinas, A. Vayonakis, P. Day, B. Mazin, and H. Leduc, Equivalence of the effects on the complex conductivity of superconductor due to temperature change and external pair breaking, J. Low Temp. Phys. **151**, 557 (2008).

[8] A. J. Annunziata, D. F. Santavicca, L. Frunzio, G. Catelani, M. J. Rooks, A. Frydman, and D. E. Prober, Tunable superconducting nanoinductors, Nanotechnology **21**, 445202 (2010).

[9] D. C. Mattis and J. Bardeen, Theory of the anomalous skin effect in normal and superconducting metals, Phys. Rev. **111**, 412 (1958).

[10] W.-K. Kwok, U. Welp, A. Glatz, A. E. Koshelev, K. J. Kihlstrom, and G. W. Crabtree, Vortices in high-performance high-temperature superconductors, Rep. Prog. Phys. **79**, 116501 (2016).

[11] N. Kopnin, *Theory of Nonequilibrium Superconductivity*, International Series of Monographs on Physics (Oxford University Press, 2001).

[12] E. Silva, N. Pompeo, and O. V. Dobrovolskiy, Vortices at microwave frequencies, Phys. Sci. Rev. **2**, 20178004 (2017).
[13] J. Villegas, E. Gonzalez, M. Gonzalez, J. V. Anguita, and J. Vicent, Experimental ratchet effect in superconducting films with periodic arrays of asymmetric potentials, Phys. Rev. B **71**, 024519 (2005).
[14] C. W. J. Beenakker and H. van Houten, Josephson current through a superconducting quantum point contact shorter than the coherence length, Phys. Rev. Lett. **66**, 3056 (1991).
[15] G. Kimmel, I. A. Sadovskyy, and A. Glatz, In silico optimization of critical currents in superconductors, Phys. Rev. E **96**, 013318 (2017).
[16] M. Tinkham, Viscous flow of flux in type-II superconductors, Phys. Rev. Lett. **13**, 804 (1964).
[17] S. Rasmussen, K. Christensen, S. Pedersen, L. Kristensen, T. Bækkegaard, N. Loft, and N. Zinner, Superconducting circuit companion—An introduction with worked examples, PRX Quantum **2**, 040204 (2021).
[18] K. Likharev and V. Semenov, RSFQ logic/memory family: A new Josephson-junction technology for sub-terahertz-clock-frequency digital systems, IEEE Trans. Appl. Supercond. **1**, 3 (1991).
[19] J. Aumentado, Superconducting parametric amplifiers: The state of the art in Josephson parametric amplifiers, IEEE Microw. Mag. **21**, 45 (2020).
[20] D. V. Morozov, A. Casaburi, and R. H. Hadfield, Superconducting photon detectors, Contemp. Phys. **62**, 69 (2021).
[21] J. Koch, M. Y. Terri, J. Gambetta, A. A. Houck, D. I. Schuster, J. Majer, A. Blais, M. H. Devoret, S. M. Girvin, and R. J. Schoelkopf, Charge-insensitive qubit design derived from the Cooper pair box, Phys. Rev. A **76**, 042319 (2007).
[22] M. Castellanos-Beltran and K. Lehnert, Widely tunable parametric amplifier based on a superconducting quantum interference device array resonator, Appl. Phys. Lett. **91**, 083509 (2007).
[23] C. Macklin, K. O'brien, D. Hover, M. Schwartz, V. Bolkhovsky, X. Zhang, W. Oliver, and I. Siddiqi, A near–quantum-limited Josephson traveling-wave parametric amplifier, Science **350**, 307 (2015).
[24] R. Di Vora, A. Lombardi, A. Ortolan, R. Pengo, G. Ruoso, C. Braggio, G. Carugno, L. Taffarello, G. Cappelli, N. Crescini, *et al.*, Search for galactic axions with a traveling wave parametric amplifier, Phys. Rev. D **108**, 062005 (2023).
[25] S. J. Lee and J. B. Ketterson, Critical sheet resistance for the suppression of superconductivity in thin Mo-C films, Phys. Rev. Lett. **64**, 3078 (1990).
[26] M. Liu and C. T. Black, Performance analysis of superconductor-constriction-superconductor transmon qubits, arXiv:2301.04276.